



A heterostructure of interlayer-expanded 1T phase MoS₂ and spherical MoO₂ for efficient and stable hydrogen evolution

Xianbo Yu^{a,*}, Feng Yan^{b,*}, Yang Zhao^a, Bo Geng^{c,*}, Xinzhi Ma^a, Lili Wu^a, Xitian Zhang^a, Yujin Chen^{b,*}

^a Key Laboratory for Photonic and Electronic Bandgap Materials, Ministry of Education, School of Physics and Electronic Engineering, Harbin Normal University, Harbin 150025, China

^b Key Laboratory of In-Fiber Integrated Optics, Ministry of Education, College of Physics and Optoelectronic Engineering, Harbin Engineering University, Harbin 150001, China

^c School of Physics and Engineering, Henan University of Science and Technology, Luoyang 471023, China



ARTICLE INFO

Keywords:

Heterostructure
Interlayer spacing expansion
Molybdenum disulfide
Molybdenum dioxide
Hydrogen evolution reaction

ABSTRACT

The inferior hydrogen evolution reaction (HER) catalytic performance of MoS₂ can be attributed to its small edge ratio, large inert substrate surface, and poor electrical conductivity, while the multiple strategies are expected to be employed simultaneously to modulate the electronic structure of MoS₂ and yield catalysts with superior HER catalytic performance. Here, we report a MoS₂ containing a 1 T phase with expanded layer spacing and construct it as a heterostructured material with MoO₂ (MoO₂ @E-MoS₂). Specifically, the presence of the 1 T phase and expanded layer structure of MoS₂ can enhance electrode conductivity, increase active site exposure, promote H₂O adsorption, and optimize the Gibbs-free energy of hydrogen. The constructed heterostructure can modulate the electronic structure of the catalyst, enhance electron transfer at the interface, elevate water adsorption energy, and reduce the hydrogen reaction energy barrier. Moreover, density functional theory calculations indicate that the S site of MoS₂ in this catalyst exhibits a higher affinity for H₂O adsorption, while the Mo site demonstrates a greater capacity for H⁺ adsorption/desorption. Ultimately, MoO₂ @E-MoS₂ shows low overpotentials of 93 and 99 mV at a current density of 10 mA cm⁻², as well as exceptional long-term stabilities exceeding 70 and 130 h at current densities ranging from 10 to 30 mA cm⁻² in acidic and alkaline media, respectively.

1. Introduction

Hydrogen energy, as a clean and renewable fuel with high calorific value, is one of the ideal substitutes for traditional fossil energy [1]. Electrocatalytic hydrogen generation is thought to be a feasible preparation technique with high purity and straightforward operation. However, due to their high cost and poor long-term durability, catalysts with better hydrogen evolution reaction (HER) performance, such as Pt-based catalysts, are inappropriate for large-scale industrial manufacturing [2,3]. Therefore, the creation of effective and reliable non-precious metal catalysts is required. Molybdenum disulfide (MoS₂) is regarded as the best prospective catalyst to replace Pt-based materials due to its high element abundance, tunable electronic structure, and exceptional chemical stability [4,5]. However, MoS₂ typically exhibits suboptimal performance because of its small proportion of edges, large inert basal planes, and poor electrical conductivity [6–8]. In the past

decade, extensive research has been conducted on improving HER catalytic activity of MoS₂-based materials, including heterojunction interface structure [9–11], phase engineering [11–13], defect design [4,12,14,15], elemental doping [14,16,17], nanostructure design [6,18,19], or incorporating MoS₂ with conductive materials [11,20,21]. Despite striking achievements, the activity and stability of MoS₂-based catalysts still face numerous practical challenges that need to be addressed.

Generally, implementing one of the aforementioned strategies may lead to some performance enhancement; however, its efficacy is limited and does not result in significant improvement [10–12,14,16,22]. Therefore, it is recommended to employ two or more strategies simultaneously. Shi *et al.* fabricated a non-uniform interface between MoS₂ and MXene to enhance the intrinsic HER activity of MoS₂ in alkaline electrolytes, however, the results were unsatisfactory. By introducing Co into the MoS₂ lattice to induce a phase transition and optimize the hydrogen adsorption/desorption, significant improvement was

* Corresponding authors.

E-mail addresses: ge_yuxianbo@126.com (X. Yu), yanfeng@hrbeu.edu.cn (F. Yan), gengbo@hrbeu.edu.cn (B. Geng), chenyujin@hrbeu.edu.cn (Y. Chen).

observed in HER performance [10]. It is evident that the simultaneous implementation of multiple strategies led to catalysts exhibiting superior catalytic performance [10–12,14,16,22]. Currently, the construction of MoS₂-based heterostructural catalysts can improve the HER catalytic activity because they tend to have better physicochemical properties than individual components [8–11,18,22]. The charge transfer at the heterojunction interface leads to the redistribution of electrons, which can tune the electronic structure of the material [8,9]. For example, the MoS₂/SnS₂ heterostructure designed by Sun *et al.* can enhance the water adsorption capacity of the edge and base of MoS₂, hence enhancing the catalyst's intrinsic catalytic efficiency and active surface area [8]. Although MoS₂-based heterostructures can improve charge transfer efficiency and optimize the adsorption states of reaction intermediates, their essence does not alter the structure of MoS₂ itself. As a result, both electrode conductivity and kinetic processes remain inadequate for practical applications [11]. Therefore, regulating the structure of MoS₂ itself in MoS₂-based heterostructure is also a crucial aspect to consider.

Recently, researchers have found that regulating the interlayer spacing of MoS₂ plays an vital role in improving HER catalytic ability [17,19,20]. According to Lan *et al.*, this increased MoS₂ interlayer spacing (from 0.62 nm to 0.95 nm) can offer a significant increase in active sites and more channels to accelerate the electron transfer of HER, which can significantly reduce the ΔG_{H^*} from –0.201 eV to –0.052 eV [20]. Moreover, the density of states (DOS) simulation demonstrates that the increase of interlayer spacing (from 0.62 nm to 0.94 nm) can modify the edge electronic structure of MoS₂, shifting the *d*-band center by 0.1 eV to the Fermi level, which is beneficial to strengthen the hydrogen adsorption and increase hydrogen coverage on the edge sites [19]. In addition, unlike 2 H phase MoS₂ (2 H-MoS₂), 1 T phase MoS₂ (1 T-MoS₂) with octahedral structure has some characteristics that are beneficial to HER, such as proliferation reaction sites and metal properties on the base surface [11–13,23–26]. The metal phase 1 T-MoS₂ has better conductivity, which can improve the electron transport in the catalytic process and promote the kinetic process of electrolytic water, thereby enhancing the HER catalytic performance [11–13,23–26]. So far, the synthesis of layered MoS₂ primarily relies on solvothermal methods ("bottom-up"), while the synthesis strategy for achieving the 1 T-MoS₂ mostly involves a stripping-induced reconfiguration approach ("top-down"), which often requires harsh synthesis conditions and results in low yields [27,28]. Therefore, developing a simultaneous synthesis method for MoS₂-based heterostructures that can achieve both an expanded layer structure and the 1 T phase is crucial to enhancing the catalytic efficiency of HER for the entire electrode.

Herein, we prepared interlayer expanded MoS₂ (E-MoS₂) containing 1 T phase and constructed it with MoO₂ to form a heterostructure material (MoO₂ @E-MoS₂) by the solvothermal method and heat treatment strategy. Among them, structural characterization, electrochemical performance test, and density functional theory (DFT) calculations prove that the constructed heterostructure can change the electronic structure of the catalyst, accelerate the transfer of electrons at the interface, increase the water adsorption energy (ΔE_{H2O}), and optimize the free energy of hydrogen adsorption (ΔG_H^*). The 1 T phase and the expanded layer spacing of MoS₂ can increase the conductivity of the electrode, increase the number of exposed active sites, elevate the ΔE_{H2O} , and optimize the ΔG_{H^*} . DFT calculations reveal that the S site of MoS₂ in MoO₂ @E-MoS₂ exhibits a higher affinity towards H₂O adsorption, while the Mo site is more favourable for H^{*} adsorption/desorption. The HER catalytic performance was synergistically enhanced through the implementation of various strategies, including building heterogeneous structures, designing expanded layer structures, and synthesizing 1 T-MoS₂. As a result, MoO₂ @E-MoS₂ exhibits superior HER catalytic activity with the overpotentials of only 93 and 99 mV at a current density of 10 mA cm^{–2} in 0.5 M H₂SO₄ and 1.0 M KOH, respectively. Additionally, this catalyst also exhibits outstanding long-term stability in acid and alkaline media, and the current loss is

negligible after continuous catalysis for 70 and 130 h at the current densities of 10–30 mA cm^{–2}, indicating its great potential for large-scale application in electrocatalytic hydrogen production.

2. Experimental section

2.1. Chemicals

Glycerol (C₃H₈O₃, AR, 99%), isopropanol (C₃H₈O, AR, 99.7%), thiourea (CH₄N₂S, ≥99.0%), and MoCl₅ (99.6%) were purchased from Shanghai Aladdin biochemical technology co., LTD (China). Moreover, all the relevant reagents in this work were not further purified except potassium hydroxide aqueous electrolyte.

2.2. Synthesis of MoGs

Mo-glycerate spheres (MoGs) were synthesized as follow: firstly, 20 mL of glycerol was dispersed in 50 mL of isopropanol. After stirred for 20 min, 100 mg of MoCl₅ was added to the above solution. Then, the resulting solution was transferred into the teflon-lined stainless steel autoclave and heated to 200 °C for 3 h. After cooling down, the dark brownish products were centrifuged and washed with water and ethanol, and then dried in a vacuum oven at 60 °C overnight.

2.3. Synthesis of MoO₂ and MoO₂@E-MoS₂

To obtained the MoO₂ nanospheres, the MoGs were subjected to direct heating at 450 °C for a duration of 2 h in an Ar flow. Regarding the synthesis of MoO₂ @E-MoS₂, the following procedure is employed. 60 mg of MoO₂ was dissolved in 60 mL mixture solution (36 mL absolute ethanol and 24 mL distilled water), and then 650 mg of thiourea was added. After stirring for 20 min, the obtained solution was transferred into teflon-lined autoclave and treated at 180 °C for 24 h. The autoclave was cooled down to room temperature naturally, and the precipitates were collected and washed by absolute ethanol and distilled water. After dried in a vacuum oven at 60 °C overnight, the MoO₂ @E-MoS₂ was obtained.

2.4. Synthesis of MoO₂@MoS₂ and E-MoS₂

MoO₂ @MoS₂ was synthesized by directly thermal treatment of MoO₂ @E-MoS₂ under 600 °C for 2 h in H₂/Ar flow. Moreover, in comparison to MoO₂ @E-MoS₂, E-MoS₂ was synthesized using identical conditions except for the substitution of 60 mg of MoO₂ with 60 mg of MoGs.

2.5. Synthesis of MoO₂@E-MoS₂-170, MoO₂@E-MoS₂-180, MoO₂@E-MoS₂-190, and MoO₂@E-MoS₂-220

As previously mentioned, the synthesis of sample MoO₂ @E-MoS₂ was achieved through a 24 h heat treatment in a teflon-lined autoclave at 180 °C (designated as MoO₂ @E-MoS₂-180). To confirm the superior catalytic performance of 1 T-MoS₂ over HER, we also synthesized MoO₂ @E-MoS₂ with varying mass ratios of 2 H and 1 T phases through precise control of reaction temperatures at 170, 190, and 220 °C under the identical conditions (designated as MoO₂ @E-MoS₂-170, MoO₂ @E-MoS₂-190, and MoO₂ @E-MoS₂-220).

2.6. Electrochemical measurements

The electrochemical performances of the catalysts were evaluated in N₂ saturated 0.5 M H₂SO₄ or 1.0 M KOH solutions using a three-electrode cell system connected with the potentiostat. A carbon rod and Ag/AgCl electrode (in acidic medium) or saturated calomel electrode (in alkaline medium) were used as the counter and reference electrodes, respectively. The carbon fiber papers were utilized as

working electrodes with a loading mass of 1.5 mg cm^{-2} . The linear sweep voltammetry (LSV) curves were obtained at a scan rate of 5 mV s^{-1} . Cyclic voltammetry (CV) was employed to investigate the double-layer capacitance (C_{dl}) at non-faradaic potentials ranging from 0.05 V to 0.15 V versus reversible hydrogen electrode (RHE), which enabled us to estimate the effective electrochemical surface area (ECSA) with high accuracy. The frequency range of 0.1 Hz to 100 kHz was utilized for the measurement of Electrochemical Impedance Spectroscopy (EIS). The turnover frequency (TOF) was calculated by the measured cyclic voltammetry (CV) curves in the phosphate buffer solution ($\text{pH} = 7$) with the scan rate of 50 mV s^{-1} . The relevant equations are as follows: $\text{TOF (s}^{-1}\text{)} = j / 2nF$ and $n (\text{mol}) = Q / 2F$, where n represents the number of active sites, j is the current density, F represents the Faraday constant, and Q is the voltammetric charges. All measured potentials were corrected against the RHE reference electrode using the Nernst equation: $E_{\text{RHE}} = E_{\text{Ag}/\text{AgCl}} + 0.059 \times \text{pH} + 0.197 \text{ V}$; $E_{\text{RHE}} = E_{\text{Hg}/\text{Hg}_2\text{Cl}_2} + 0.059 \times \text{pH} + 0.241 \text{ V}$. In order to detect the Faradaic efficiency, the H_2 concentrations were measured using gas chromatography (Trace 1300 GC) equipped with Molecular sieve 5 \AA capillary column and thermal conductivity detector. During the water electrolysis, the change in the amount of H_2 produced can be recorded after 5 min of electrolysis each time. The current densities were kept at 44 and 61 mA cm^{-2} in acidic and alkaline media with volume flow rates of 0.16 and 0.22 sccm , respectively.

2.7. Structure characterizations

The morphology and structure of all the catalysts were observed by scanning electron microscope (Hitachi SU8010, 15 kV) and transmission electron microscopy, (Tecnai G² F30, 300 kV). The crystal structure of catalysts was characterized by X-ray diffractometer (PANalytical X'Pert PRO) with $\text{Cu K}\alpha$ radiation ($\lambda = 1.5418 \text{ \AA}$) at 40 kV . X-ray photoelectron spectroscopy was characterized to analyze the chemical compositions by using a spectrometer with $\text{Al K}\alpha$ radiation (Nepean, ON) and Renishaw INVIA. The amount of the collected H_2 was tested with Thermo Scientific TRACE 1300.

2.8. Computational details

All calculations were performed within the Density Functional Theory (DFT) framework, and the electronic and electocatalytic properties of materials were investigated by using the CASTEP module implemented in Material Studio. The generalized gradient approximation (GGA) with a Perdew-Burke-Ernzerhof (PBE) functional was used to describe the electronic exchange and correlation effects, and the plane-wave cutoff was tested and set to 400 eV . The self-consistent field (SCF) tolerance was $1 \times 10^{-5} \text{ eV}$. The Brillouin zone was sampled at a $(2 \times 2 \times 1)$ mesh. The core electrons were treated by the ultrasoft pseudopotential. MoO_2 (-111) surfaces were modeled by the periodically repeated slabs with (1×1) unit cells, and MoS_2 (002) surface was modeled by the periodically repeated slabs with (3×2) unit cells. The $\text{MoO}_2/\text{MoS}_2$ heterojunction was constructed with a vacuum layer of 15 \AA , which was introduced to avoid interactions between simulated two adjacent simulated layers. Considering the different adsorption energies on different sites, various potential adsorption sites were taken into account in the calculations, while only the most stable binding sites were adopted as the real active sites.

The water adsorption energies ($\Delta E_{\text{H}_2\text{O}}$) at the sample of surfaces were calculated by the equation of $\Delta E_{\text{H}_2\text{O}} = E_{\text{surf+H}_2\text{O}} - E_{\text{surf}} - E_{\text{H}_2\text{O}}$, where the E_{surf} and the $E_{\text{surf+H}_2\text{O}}$ are the total energies of the surface before and after water adsorption, and $E_{\text{H}_2\text{O}}$ is the energy of a free water. The Gibbs free energies for hydrogen adsorption (ΔG_{H^*}) were calculated from the equation: $\Delta G_{\text{H}^*} = \Delta E_{\text{H}^*} + \Delta ZPE - T\Delta S$, where the ΔE_{H^*} , ΔZPE , T , and ΔS represent the binding energy, zero point energy change, temperature, and entropy change of H^* adsorption system, respectively. As the entropy of hydrogen in absorbed state is negligible, ΔS can be

calculated as $-1/2 S_0$ (S_0 is the entropy of H_2 in the gas phase at standard conditions, 1 bar of H_2 and $\text{pH} = 0$ at 300 K).

3. Results and discussion

3.1. Composition and structure

The synthesis process of $\text{MoO}_2@\text{E-MoS}_2$ was divided into three distinct steps. As depicted in Fig. 1a, firstly, uniform Mo-glycerate spheres (MoGs) were synthesized via a solvothermal method and using glycerol and isopropanol together as the mixed solvent and MoCl_5 as the molybdenum source. Secondly, MoGs underwent heat treatment in an Ar atmosphere to achieve uniform sizing of MoO_2 spheres. Thirdly, sulfurization was performed on the MoO_2 to create a heterogeneous structure with inner-layered MoO_2 and outer-layered MoS_2 nanosheets. Meanwhile, the (002) interplanar distance of MoS_2 was expanded and the crystalline phase consisted of a mixture of 1 T and 2 H phase. In order to reflect the synergistic advantages of the preparation of $1 \text{ T}/2 \text{ H}$ mixed-phase MoS_2 with expanded layer spacing and the constructed heterogeneous structure, three additional samples were prepared in this paper: i) pure MoO_2 nanospheres (MoO_2); ii) direct sulfidation of MoGs results in the formation of $1 \text{ T}/2 \text{ H}$ mixed-phase MoS_2 nanospheres featuring an expanded (002) interplanar distance, denoted as E-MoS_2 ; iii) heat treatment of $\text{MoO}_2 @\text{E-MoS}_2$ under Ar/ H_2 atmosphere results in the formation of heterostructured nanospheres of 2 H-MoS_2 (without layer expansion) and MoO_2 ($\text{MoO}_2 @\text{MoS}_2$). As depicted in Fig. 1b and Fig. S1a, the X-ray diffraction (XRD) patterns exhibit that all MoO_2 diffraction peaks conform to JCPDs no. 76–1807, indicating the transformation of MoGs into MoO_2 after thermal treatment. For E-MoS_2 , all the diffraction peaks correspond to the $1 \text{ T}/2 \text{ H}$ mixed-phase (JCPDs no. 37–1492 and simulated 1 T-MoS_2) except for the (002) crystal plane. Notably, the peak positions of the 1 T-MoS_2 were simulated, and the detailed parameters are presented in Table S1. In addition, the (002) crystal plane peaks of E-MoS_2 at 9.49° deviate from the standard position of 14.3° , indicating an expansion in interplanar distance from 0.62 nm to 0.93 nm . Similarly, the construction of a heterojunction between E-MoS_2 and MoO_2 results in an expanded (002) crystalline plane spacing of MoS_2 , as evidenced by the XRD pattern of $\text{MoO}_2 @\text{E-MoS}_2$. Moreover, in order to demonstrate the presence of $1 \text{ T}/2 \text{ H}$ mixed-phase MoS_2 in both $\text{MoO}_2 @\text{E-MoS}_2$ and E-MoS_2 , XRD measurements were also conducted. As depicted in Fig. S1a, the obtained $\text{MoO}_2 @\text{MoS}_2$ exclusively exhibits the stable 2 H-MoS_2 due to high temperature heat treatment, which corresponds to the standard card of hexagonal crystalline phase MoS_2 (JCPDs no. 37–1492). Furthermore, in $\text{MoO}_2 @\text{E-MoS}_2$, apart from the dominant 2 H-MoS_2 , there are two additional peaks at 31.8° and 56.6° that correspond to the simulated peaks of 1 T-MoS_2 . This observation confirms the presence of a mixed $1 \text{ T}/2 \text{ H}$ phase in both synthesized $\text{MoO}_2 @\text{E-MoS}_2$ and E-MoS_2 . Additionally, the enlargement of the (002) crystalline plane spacing is primarily attributed to incomplete sulfidation during the low-temperature reaction, resulting in residual Mo-O bonds ($\text{MoO}_x(\text{OH})_y$) between the MoS_2 layers that support interlayer MoS_2 [29,30]. In order to demonstrate above conclusion, E-MoS_2 was annealed at $500 \text{ }^\circ\text{C}$ under Ar flow. As shown in Fig. S1b, the appearance of MoO_2 further verifies the oxygen incorporation, because the incorporated O element should be the only source of MoO_2 .

The elemental composition and chemical bonding states of the four material surfaces were investigated by using X-ray photoelectron spectroscopy (XPS) analysis. For the high-resolution Mo 3d spectrum, the presence of two spectral peaks at 229.6 and 232.8 eV unequivocally indicates that MoS_2 in $\text{MoO}_2 @\text{MoS}_2$ exclusively adopts a 2 H phase configuration [21]. As shown in Fig. 1c, the two spectral peaks located at 228.9 and 232.0 eV correspond to the $\text{Mo 3d}_{5/2}$ and $\text{Mo 3d}_{3/2}$ orbitals of MoS_2 in the 1 T phase, which unequivocally indicates that the MoS_2 in $\text{MoO}_2 @\text{E-MoS}_2$ and E-MoS_2 is a $1 \text{ T}/2 \text{ H}$ mixed-phase [31]. Moreover, in contrast to the $\text{MoO}_2 @\text{MoS}_2$ material, the Mo 3d spectrum of both

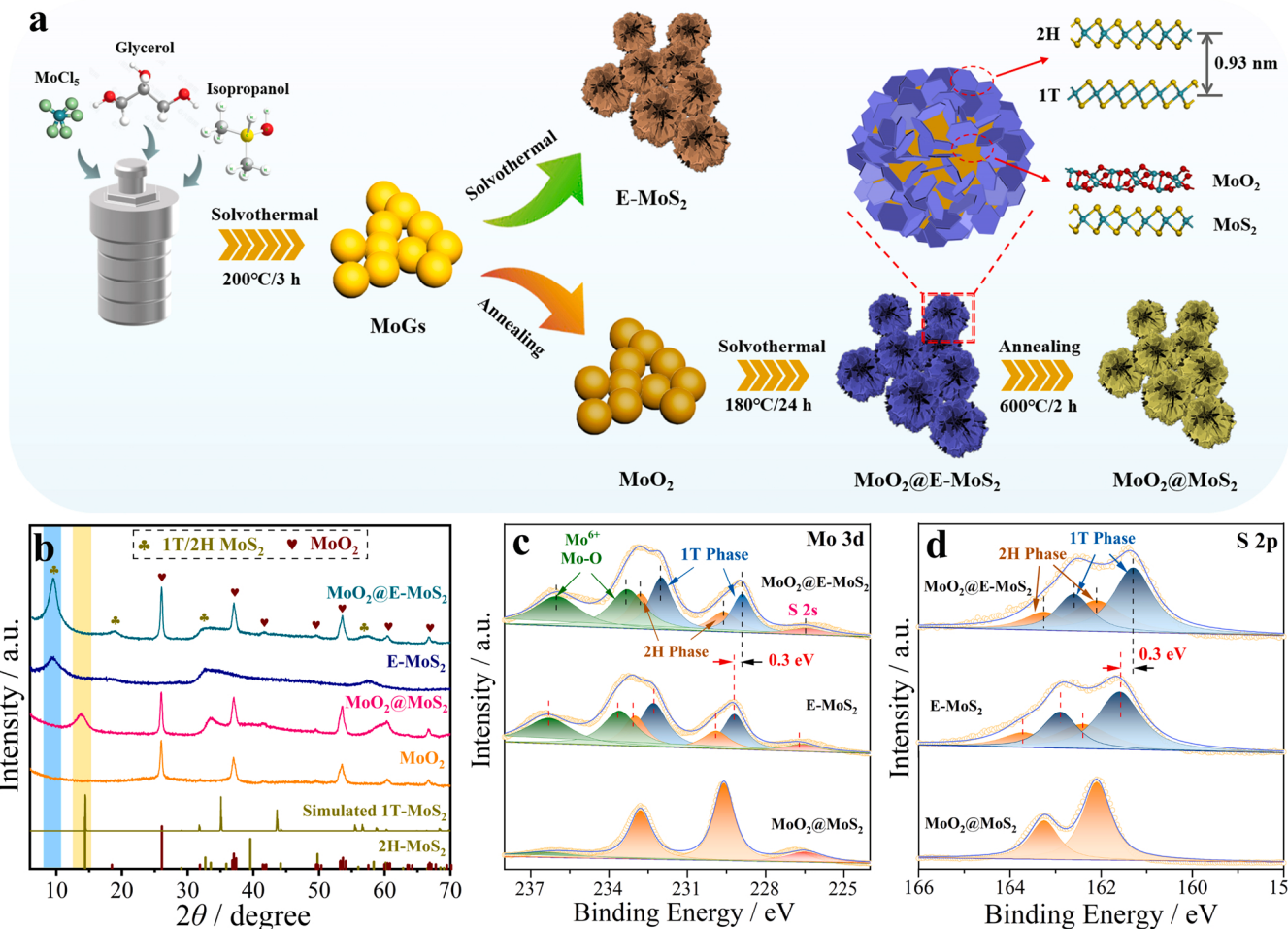


Fig. 1. a) Schematic illustration and b) XRD patterns of MoO_2 @E-MoS₂, MoO_2 @MoS₂, E-MoS₂ and MoO_2 . XPS spectra of c) Mo 3d and d) S 2p of MoO_2 @E-MoS₂, MoO_2 @MoS₂, and E-MoS₂.

E-MoS₂ and MoO_2 @E-MoS₂ exhibit larger peak areas (corresponding to Mo^{6+}) for the two Mo–O bonds with binding energies at 233.3 and 236.0 eV, providing further evidence of oxygen doping within the expanded interlamination of MoS₂ [29,30]. Further analysis was conducted on the high-resolution spectra of S 2p. The two spectral peaks observed at positions 162.1 and 163.6 eV in Fig. 1d are attributed to the presence of the 2 H-MoS₂, while the peaks detected at 161.3 and 162.6 eV are associated with the orbital peaks S 2p_{3/2} and S 2p_{1/2} of the 1 T-MoS₂ [31]. The findings above further demonstrate the coexistence of both 1 T and 2 H phases of MoS₂ in MoO_2 @E-MoS₂ and E-MoS₂, whereas only the formation of 2 H-MoS₂ is observed in MoO_2 @MoS₂ after annealing. It is noteworthy that all the spectral peak positions of MoO_2 @E-MoS₂ are shifted towards lower binding energy positions compared to E-MoS₂, demonstrating that the construction of the heterostructure enables the existence of electronic interactions between MoO_2 and MoS₂, with electron transfer from MoO_2 to MoS₂. Additionally, Fig. S1c,d display the high-resolution spectra of Mo 3d and O 1s for the pure MoO_2 sample, revealing the presence of both Mo^{4+} and Mo–O species that confirm the successful synthesis of MoO_2 . The appearance of Mo^{6+} is primarily attributed to the surface oxidation of the MoO_2 .

The microscopic morphology and structure of MoO_2 @E-MoS₂, MoO_2 @MoS₂, E-MoS₂ and MoO_2 were analyzed using scanning electron microscopy (SEM) and transmission electron microscopy (TEM) to provide a comprehensive understanding of their properties. The SEM images in Fig. S2a,b reveal that the MoGs precursors show uniform spherical morphology with smooth surfaces, exhibiting an average diameter of approximately 500 nm. After undergoing heat treatment,

the MoGs were transformed into spherical MoO_2 . In comparison with the MoGs, low magnification SEM analysis (Fig. S3a) reveals no significant alteration in the morphology of MoO_2 nanospheres, which remain uniform in size. However, upon further magnification, surface roughness is observed on MoO_2 (Fig. S3b,c). High-resolution TEM (HRTEM) analysis in Fig. S3d reveals that the MoO_2 nanospheres exhibit the lattice spacings of 0.34 and 0.17 nm, corresponding to the (−111) and (211) crystal planes in the MoO_2 (JCPDs no. 76–1807), thus confirming successful synthesis of MoO_2 after heat treatment. As illustrated in Fig. 2a–c, the MoO_2 nanospheres underwent sulfidation and experienced a morphological transformation, resulting in the formation of MoO_2 @E-MoS₂ nanospheres with a surface composed of numerous nano-scale lamellar layers and an enlarged diameter of approximately 600 nm. Moreover, Fig. 2c shows the selected area electron diffraction pattern of MoO_2 @E-MoS₂. The lattice spacings of 2 H-MoS₂ (0.12 and 0.27 nm) and 1 T-MoS₂ (0.16 and 0.21 nm) can be identified, further confirming the coexistence of a 1 T/2 H mixed-phase MoS₂ in the sample MoO_2 @E-MoS₂.

The lattice stripe of MoO_2 @E-MoS₂ is discernible in the HRTEM image (Fig. 2d), with an interplanar distance of approximately 0.93 nm. This interplanar distance is consistent with the layer spacing value obtained from XRD test results, indicating successful preparation of expanded MoS₂ layer spacing. Additionally, the HRTEM image in Fig. 2e revealed the existence of a 1 T phase possessing a triangular coordination octahedral structure and a 2 H phase featuring a honeycomb triangular cone structure within the material, thereby demonstrating the presence of a hybrid 1 T/2 H phase. It is noteworthy that the lattice

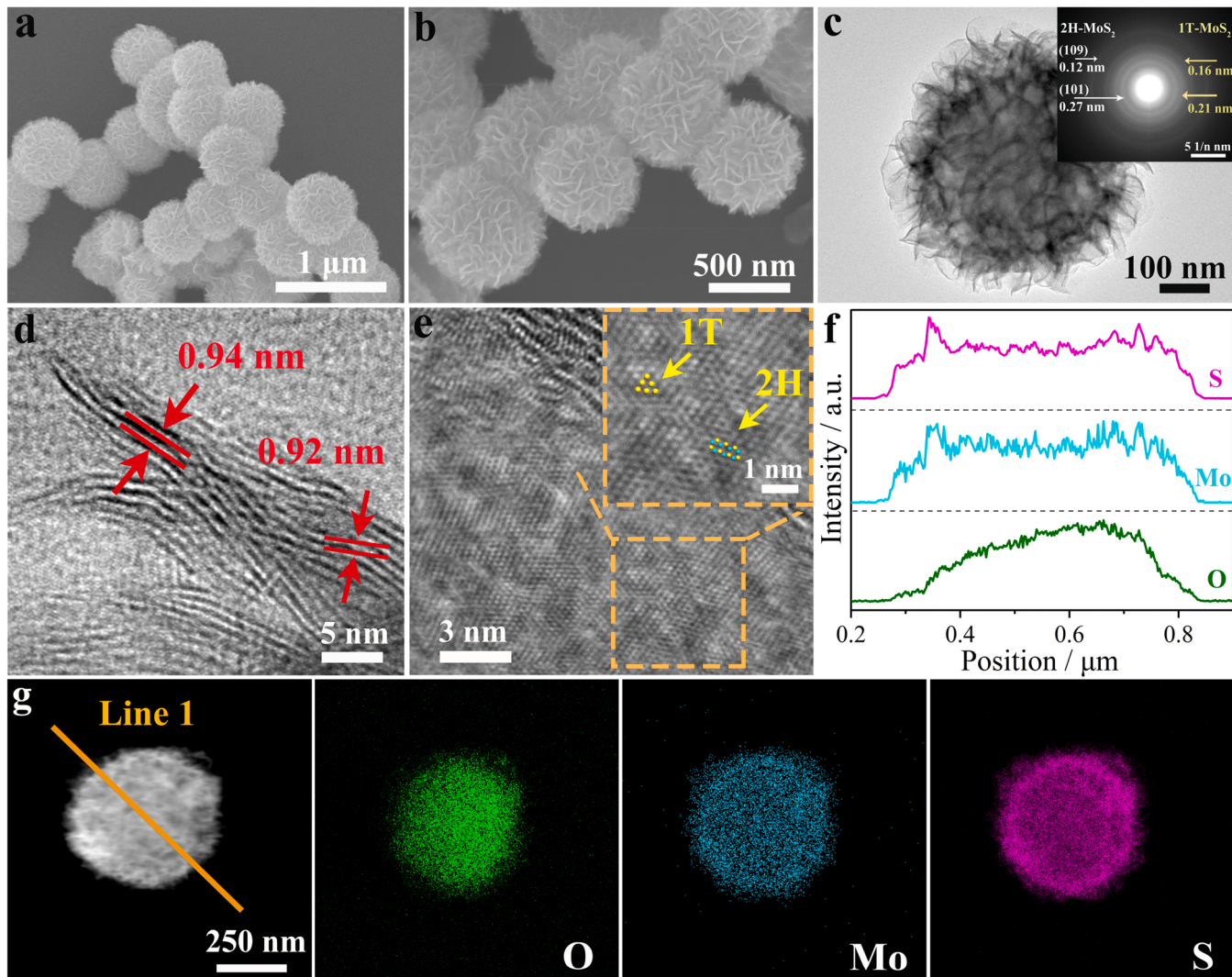


Fig. 2. a,b) SEM, c) TEM, d,e) HRTEM images of MoO_2 @E-MoS₂. f) The corresponding linear scanning and g) EDS element mapping images of an individual MoO_2 @E-MoS₂ nanosphere. The inset in c) is the selected area electron diffraction pattern of MoO_2 @E-MoS₂.

structure of MoO_2 is scarcely discernible in the HRTEM image, which can be ascribed to the dispersed distribution of MoO_2 within the nanospheres. The thickness of the outer nanosheets in MoO_2 @E-MoS₂ spheres obscures the internal MoO_2 lattice, rendering it undetectable by TEM. To further illustrate the architecture of the MoO_2 @E-MoS₂ sphere, which features an inner core of MoO_2 and outer layers of MoS₂ nanosheets, we conducted a TEM line scan analysis to examine its elemental distribution. As depicted in Fig. 2f,g, it is evident that O is predominantly concentrated within the central region of the sphere, while S and Mo are prominently distributed along its periphery despite being present throughout. Therefore, based on the XRD pattern, it can be inferred that MoO_2 @E-MoS₂ possesses a heterogeneous structure with MoO_2 in the inner layer and MoS₂ in the outer layer. In addition, we also examined the SEM and TEM of MoO_2 @MoS₂ and E-MoS₂. As depicted in Fig. S4a-c, MoO_2 @MoS₂ exhibits a similar morphology to MoO_2 @E-MoS₂. However, the HRTEM image (Fig. S4d) reveals that the lattice spacing of MoS₂ in MoO_2 @MoS₂ is approximately 0.64 nm, indicating a transformation in crystal structure following H₂/Ar heat treatment of MoO_2 @E-MoS₂ and removal of interlayer oxygen resulting in layer spacing contraction. It should be noted that the layer spacing of MoO_2 @MoS₂ is slightly higher than that of intrinsic MoS₂ (0.62 nm), which is consistent with the characteristics of nanosized MoS₂ and in agreement with previously reported results [31]. Although E-MoS₂ exhibits a similar

nanosphere morphology to MoO_2 @E-MoS₂, TEM line scan analysis reveals that the distribution of Mo and S elements is uniform throughout the nanosphere, indicating the absence of heterogeneous structures of MoO_2 and MoS₂ in E-MoS₂ (Fig. S5a-e). Moreover, the HRTEM image in (Fig. S5c) reveal that the interplanar distance of E-MoS₂ material is 0.93 nm, indicating its expanded layer structure.

Furthermore, to determine the contents of MoS₂ and MoO₂ in MoO_2 @E-MoS₂, thermogravimetric (TG) and differential scanning calorimeter (DSC) curves of MoO_2 , E-MoS₂, and MoO_2 @E-MoS₂ were measured. As depicted in Fig. S6a,b, TG curves of MoO_2 and E-MoS₂ can calculate the carbon content in these materials ranges from 15.0 to 15.4 wt%. In addition, since MoO_2 @E-MoS₂ utilize MoO_2 as a precursor and undergo complete vulcanization to form MoS₂ over 220 °C, the carbon content of this sample lies between that of pure MoO_2 and E-MoS₂. For the convenience of calculation, the carbon content of 15.2 wt % in this sample was chosen. As a result, by using the TG curve of MoO_2 @E-MoS₂ can calculate the content of MoO₂ is 13.3 wt% (Fig. S6c). Moreover, the DSC curves of MoO_2 and E-MoS₂ reveal that the oxidation process of MoS₂ initiates at temperatures exceeding 200 °C, while the oxidation process of MoO_2 commences at temperatures higher than 300 °C. Additionally, the combustion of carbon content begins at temperatures above 350 °C, resulting in a decrease in mass. In addition, Brunauer-Emmett-Teller (BET) surface areas of MoO_2 @E-MoS₂, MoO_2

@MoS₂, E-MoS₂, and MoO₂ were measured. As shown in Fig. S7a-d, the specific surface area of 18.6 m² g⁻¹ for MoO₂ @E-MoS₂ is much larger than those of MoO₂ @MoS₂ (15.4 m² g⁻¹), E-MoS₂ (14.8 m² g⁻¹), and E-Mo₂ (5.1 m² g⁻¹), which is favorable to expose the active sites and improve HER activity.

3.2. Electrochemical process

To demonstrate the benefits of the preparation of 1 T/2 H mixed-phase MoS₂ with expanded layer spacing and the constructed heterogeneous structure, all electrodes were assessed for their HER performance in N₂-saturated acidic and basic (0.5 M H₂SO₄ and 1.0 M KOH) solutions at a sweep rate of 5 mV s⁻¹. As depicted in Fig. 3a, linear sweep voltammetry (LSV) was initially employed to evaluate the HER performance of Pt/C, MoO₂ @E-MoS₂, MoO₂ @MoS₂, E-MoS₂, and MoO₂. Undoubtedly, Pt/C exhibited the lowest onset potential (close to 0 mV) and the highest current density. For the MoO₂ @E-MoS₂, a significant current was observed at a relatively low overpotential. The current density increased rapidly with increasing potential, reaching the current density of 10 mA cm⁻² at a overpotential of 93 mV ($\eta_{10} = 93$ mV), indicating its superior HER catalytic activity. Compared to the MoO₂ @E-MoS₂, the catalytic performance of MoO₂ @MoS₂ was found to be

inferior with η_{10} of 152 mV, indicating that the 1 T/2 H mixed-phase MoS₂ with expanded layer spacing plays a crucial role in enhancing HER performance. Similarly, the catalytic performance of MoO₂ @E-MoS₂ was compared with those of E-MoS₂ and MoO₂. However, both E-MoS₂ ($\eta_{10} = 175$ mV) and MoO₂ ($\eta_{10} = 246$ mV) exhibited unsatisfactory catalytic activity when used alone, indicating that the construction of heterogeneous structures can effectively enhance the catalytic performance of HER. The Tafel slope is a crucial technique for analyzing the kinetics of catalytic reactions. Fig. 3b illustrates that the MoO₂ @E-MoS₂ displays a Tafel slope of 154 mV dec⁻¹, which is significantly lower than those of the MoO₂ @MoS₂ (183 mV dec⁻¹), E-MoS₂ (201 mV dec⁻¹), and MoO₂ (268 mV dec⁻¹), reflecting its superior charge transfer efficiency. Therefore, the lower overpotential and Tafel slope observed in Fig. 3a-c indicate that the formation of heterogeneous structures and an expanded layer of 1 T/2 H mixed-phase MoS₂ can significantly enhance electrode reaction kinetics and improve HER catalytic performance.

To gain a deeper insight into the underlying reasons for the enhanced performance of MoO₂ @E-MoS₂, we initially assessed the electrochemically active surface area (ECSA) of the electrode through electrochemical double-layer capacitance (C_{dl}). All electrodes' cyclic voltammetry (CV) curves were initially measured in the non-Faraday region at various scan rates. Subsequently, the corresponding C_{dl}

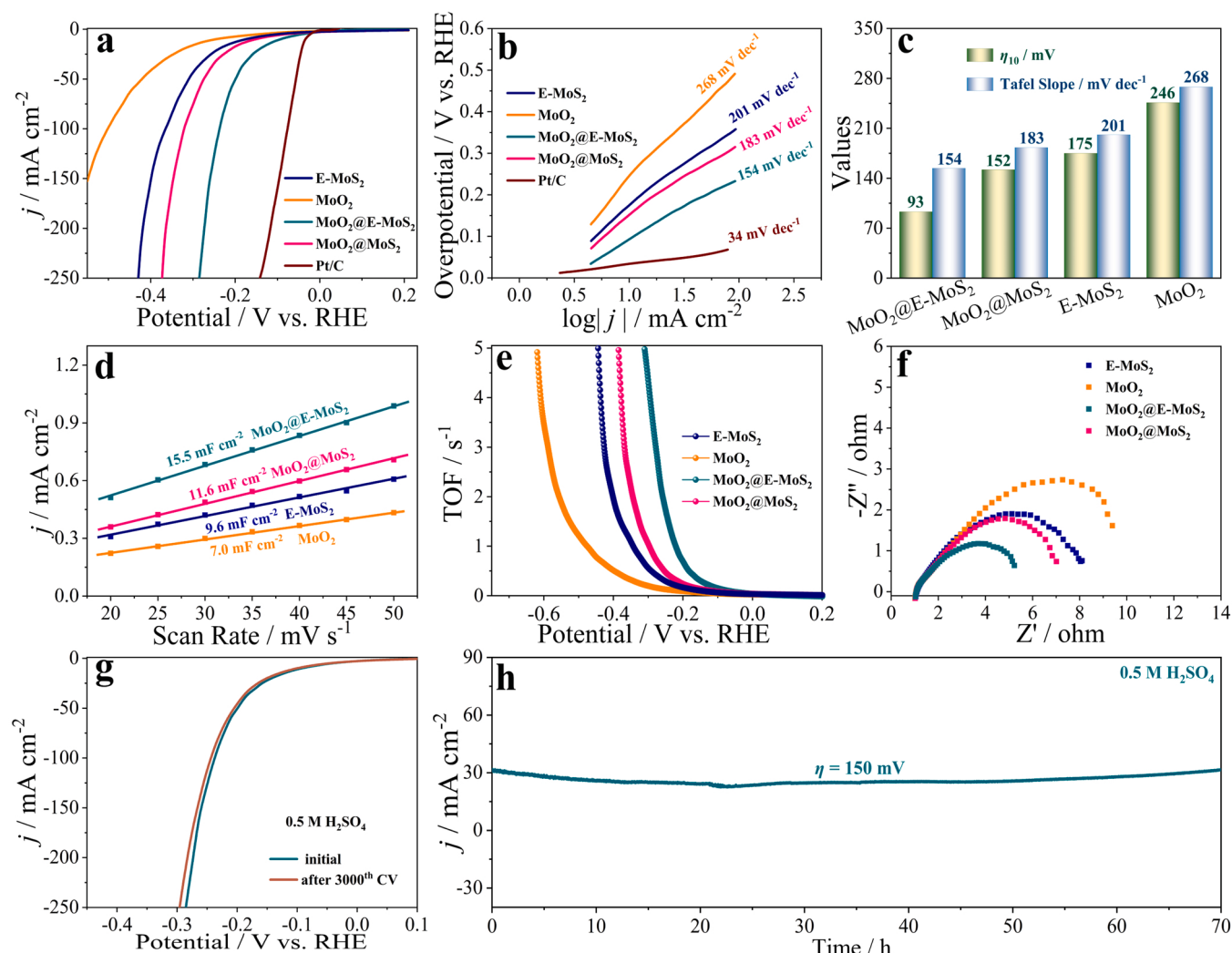


Fig. 3. a) LSV curves, b) corresponding Tafel plots, and c) histogram of η_{10} and Tafel slopes of MoO₂ @E-MoS₂, MoO₂ @MoS₂, E-MoS₂, MoO₂, and commercial Pt/C in 0.5 M H₂SO₄ solution. d) Capacitive current density as a function of scan rate, e) calculated turnover frequencies, and f) Nyquist plots of MoO₂ @E-MoS₂, MoO₂ @MoS₂, E-MoS₂, and MoO₂ in 0.5 M H₂SO₄ solution. g) LSVs of MoO₂ @E-MoS₂ before and after 3000th CV cycles and h) time-dependent current density curve under constant overpotential of 150 mV in 0.5 M H₂SO₄ solution.

values were determined by linear regression analysis. Finally, the ECSA of all materials was calculated using the equation ($ECSA = C_{dl} * A / C_s$), where A is the area of electrodes, C_s represents the capacitance of an atomically smooth surface per unit area ($40 \mu F cm^{-2}$) of the catalyst [32, 33]. The CV curves at different sweep speeds for $MoO_2 @E-MoS_2$ exhibited the largest C_{dl} ($15.5 mF cm^{-2}$), surpassing those of $MoO_2 @MoS_2$ ($11.6 mF cm^{-2}$), $E-MoS_2$ ($9.6 mF cm^{-2}$), and MoO_2 ($7.0 mF cm^{-2}$), as demonstrated in Fig. 3d and Fig. S8. Based on the aforementioned equation, the ECSAs of $MoO_2 @E-MoS_2$, $MoO_2 @MoS_2$, $E-MoS_2$, and MoO_2 were calculated to be 388 , 290 , 240 , and $175 cm^2$, respectively. $MoO_2 @E-MoS_2$ can provide a larger electrochemically active surface area, as evidenced by the increased ECSA, which is conducive to enhancing the HER catalytic performance. Normalizing the current density concerning ECSA is recommended to intuitively evaluate the catalyst's intrinsic activity. Since the surface area is proportional to the number of surface atoms, which can represent the actual number of active sites, the normalized current density serves as an approximation of each active site's activity and reflects the intrinsic activity of the catalyst. The normalized LSV curves in Fig. S9a demonstrate that $MoO_2 @E-MoS_2$ exhibits superior HER catalytic activity, as evidenced by the highest current density achieved at the same potential when compared to other samples.

Turnover frequency (TOF) was also evaluated as a crucial parameter

reflecting both catalytic activity and active site number of studied samples [34,35]. As illustrated in Fig. 3e, $MoO_2 @E-MoS_2$ exhibits the highest TOF value across the entire potential range in $0.5 M H_2SO_4$ solution. The TOF value of $MoO_2 @E-MoS_2$ reached $4.4 s^{-1}$ at an overpotential of $300 mV$, exhibiting enhancements by multiples of 4.2 , 7.8 , and 22.1 compared to those of $MoO_2 @MoS_2$, $E-MoS_2$, and MoO_2 , respectively. This result further confirms that the formation of heterogeneous structures and the expanded layer composed of mixed-phase ($1 T/2 H$) MoS_2 can effectively expose more active sites and thus improve the catalytic performance of the electrode. The electrochemical impedance spectroscopy (EIS) technique further investigated the electrode kinetic processes. As illustrated in Fig. 3f, $MoO_2 @E-MoS_2$ exhibits the lowest charge transfer resistance (R_{ct}), estimated to be $5.1 \Omega cm^{-2}$ among all tested catalysts, indicating that its structural design and components are conducive to enhancing both charge transfer and mass diffusion kinetics. The long-term stability of HER is another crucial parameter for achieving high-performance electrocatalysts. As illustrated in Fig. 3g, the LSV curve of $MoO_2 @E-MoS_2$ exhibits only a negative overpotential shift of $8 mV$ after undergoing 3000 cycles at a current density of $10 mA cm^{-2}$ compared to its original curve, indicating its remarkable durability towards HER. Moreover, the robust stability of the $MoO_2 @E-MoS_2$ is also proved by the chronopotentiometry curve at a constant overpotential of $150 mV$ and a current density of $30 mA cm^{-2}$.

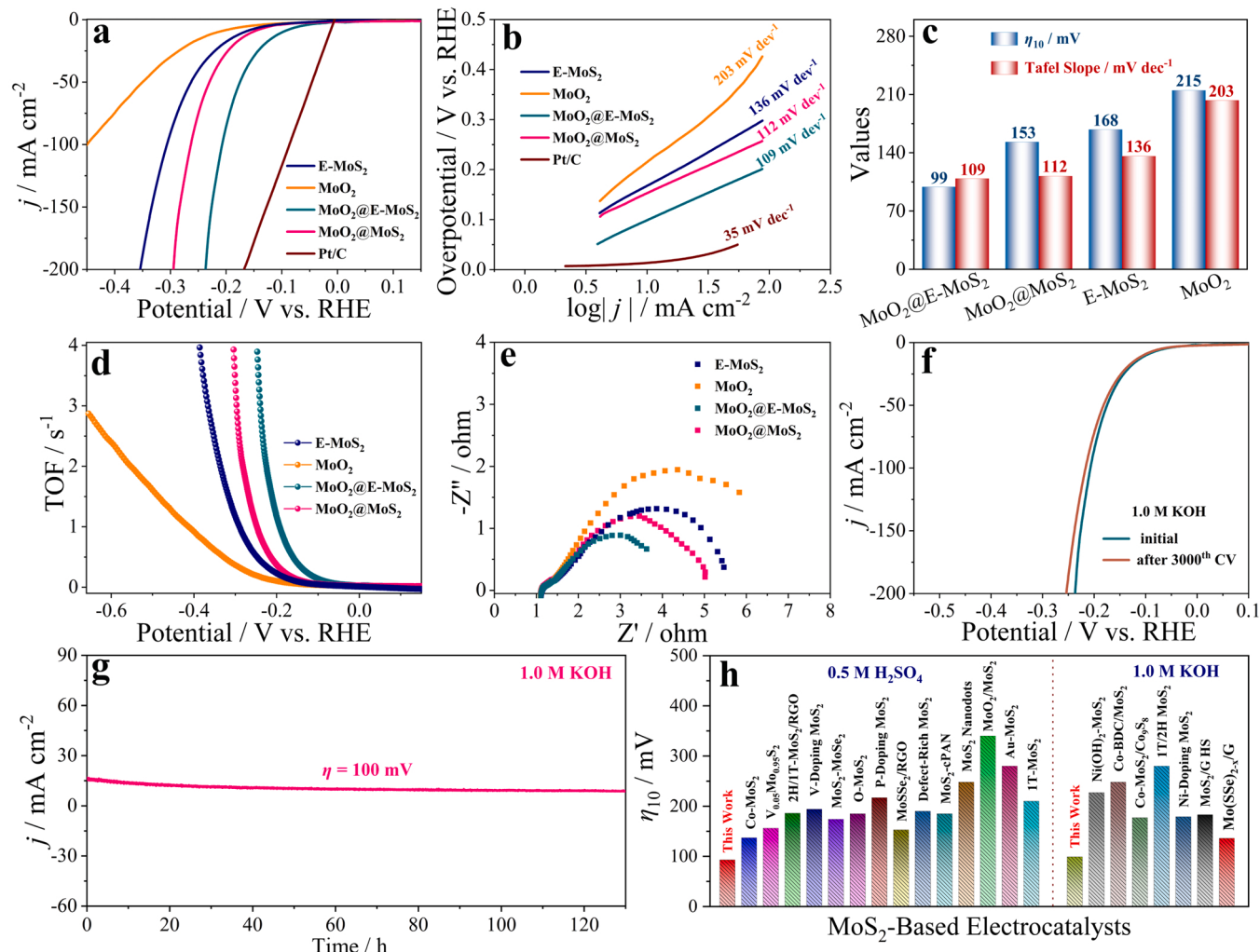


Fig. 4. a) LSV curves, b) corresponding Tafel plots, and c) histogram of η_{10} and Tafel slopes of $MoO_2 @E-MoS_2$, $MoO_2 @MoS_2$, $E-MoS_2$, MoO_2 , and commercial Pt/C in $1.0 M KOH$ solution. d) Calculated turnover frequencies and e) Nyquist plots of $MoO_2 @E-MoS_2$, $MoO_2 @MoS_2$, $E-MoS_2$, and MoO_2 in $1.0 M KOH$ solution. f) LSVs of $MoO_2 @E-MoS_2$ before and after 3000 th CV cycles and g) Time-dependent current density curve under constant overpotential of $100 mV$ in $1.0 M KOH$ solution. h) Comparison of the HER activities of $MoO_2 @E-MoS_2$ in $0.5 M H_2SO_4$ and $1.0 M KOH$ solutions with other previously reported catalysts.

in 0.5 M H₂SO₄ solution, where unobvious potential degradation is observed for electrolysis even after a long period of 70 h (Fig. 3h).

Electrochemical measurements were also conducted in alkaline solutions (1.0 M KOH), and the HER properties exhibited a similar trend to those observed under acidic conditions. To further confirm the HER catalytic ability order that, MoO₂ @E-MoS₂ > MoO₂ @MoS₂ > E-MoS₂ > MoO₂, LSV curves of all the samples were measured. As shown in Fig. 4a, MoO₂ has a negligible HER activity with the $\eta_{10} = 215$ mV. The HER catalytic performance of MoO₂ @MoS₂ was significantly enhanced by incorporating MoS₂ in the heterostructure. Similarly, the HER catalytic activity of MoO₂ @E-MoS₂ was further improved through the transformation of MoS₂ in MoO₂ @MoS₂ into expanded 1 T/2 H mixed-phase MoS₂. As a result, MoO₂ @E-MoS₂ exhibits superior HER catalytic activity with the $\eta_{10} = 99$ mV, outperformed to the MoO₂ @MoS₂ ($\eta_{10} = 153$ mV), E-MoS₂ ($\eta_{10} = 168$ mV), and MoO₂ ($\eta_{10} = 215$ mV). The Tafel slopes of all the samples were also calculated in 1.0 M KOH solution to evaluate the HER kinetics. Fig. 4b,c show that MoO₂ @E-MoS₂ has the smallest Tafel slope value than other samples, providing further evidence for the preparation of 1 T/2 H mixed-phase MoS₂ with expanded layer spacing and the formation of heterogeneous structure to enhance HER kinetics. In addition, ECSA normalized LSV curve in 1.0 M KOH solution shows that the MoO₂ @E-MoS₂ has the largest current density under the same potential (Fig. S9b). As shown in Fig. 4d, the TOF value of MoO₂ @E-MoS₂ is 5.5 s⁻¹ at an overpotential of 270 mV, more significant than those of MoO₂ @MoS₂ (1.6 s⁻¹), E-MoS₂ (0.7 s⁻¹), and MoO₂ (0.3 s⁻¹). The smallest R_{ct} of MoO₂ @E-MoS₂ (3.3 Ω cm⁻²) in alkaline electrolyte also confirms its fast electrocatalytic Faradaic process and thus a superior HER kinetics (Fig. 4e). The development of highly stable electrocatalysts is crucial for the electrodes. Therefore, we have also investigated the catalytic stability of MoO₂ @E-MoS₂ in an alkaline environment. As depicted in Fig. 4f, the LSV curve exhibited no explicit current decay even after 3000th cycles. Moreover, the MoO₂ @E-MoS₂ demonstrated remarkable stability by operating steadily for at least 130 h at an overpotential of 100 mV and a current density of 10–20 mA cm⁻². Furthermore, a comparison with other MoS₂-based materials, MoO₂ @E-MoS₂ has the lowest overpotential at a current density of 10 mA cm⁻² under both acidic and alkaline media, demonstrating that its exceptional HER catalytic performance (Fig. 4g). In addition, the Faradaic efficiency (FE) of the MoO₂ @E-MoS₂ for H₂ evolution in acidic and alkaline media were measured (Fig. S10). The measured quantity of produced H₂ is very close to the theoretically calculated H₂, and thus the calculated FE is close to 100%.

In order to investigate the morphological and structural changes of MoO₂ @E-MoS₂, MoO₂ @MoS₂, E-MoS₂, and MoO₂ electrodes after the HER test, we initially conducted stability tests in acidic and alkaline media for 5 and 30 h, respectively (with a current density set at 20 mA cm⁻²). Subsequently, these electrodes were characterized by using XRD, XPS, SEM, and TEM. As depicted in Fig. S11, XRD analysis revealed that the MoO₂ @E-MoS₂ coated carbon paper electrode maintained distinct peaks corresponding to both MoS₂ and MoO₂, consistent with those of the powder sample. Notably, even after 5 and 30 h of HER stability test in acidic and alkaline media, the diffraction peaks for both MoS₂ and MoO₂ remained pattern, indicating excellent stability of the electrode. In addition, the XRD analysis revealed the absence of any additional incidental peaks, providing evidence that no novel compounds were formed at the electrode during the HER, irrespective of the electrolyte being acidic or alkaline media. To further substantiate the aforementioned conclusion, XPS analysis was employed to investigate the structural alterations of MoO₂ @E-MoS₂ following reaction. As depicted in Fig. S12 and Fig. S13, after subjecting the MoO₂ @E-MoS₂ electrode to electrolyte treatment respectively, it can be observed from the Mo 3d and S 2p spectra that the positions and quantities of fitted peaks remained consistent with those of the original electrode material, thereby reaffirming its exceptional catalytic stability. In addition to the structural aspects, we also detected the morphology of MoO₂ @E-MoS₂, MoO₂ @MoS₂, E-MoS₂, and MoO₂ electrodes. The SEM and TEM images

in Fig. S14 and Fig. S15 demonstrate that, even after being subjected to a 5 h of HER stability test in acidic and alkaline media, the MoO₂ @E-MoS₂ electrode maintains its nanosphere morphology, with the outermost layer of MoS₂ retaining a well-defined lamellar structure. HRTEM analysis reveals that the reacted MoS₂ still exhibits an expanded interplanar distance of 0.94 nm. For MoO₂ @MoS₂ (Fig. S16 and Fig. S17) and E-MoS₂ (Fig. S18 and Fig. S19), it was able to maintain the intact morphology after 5 h of HER stability test in acidic and alkaline media, but after 30 h of testing, the MoS₂ nanosheets on the surface of the material appeared to be detached, which could potentially impact the catalytic activity and stability of the electrode for HER. As for MoO₂, its spherical morphology remained intact in both acidic and alkaline media (Fig. S20 and Fig. S21). Furthermore, HRTEM images confirmed that the lattice spacing was still measured at 0.34 nm, indicating that it was indeed MoO₂. In conclusion, MoO₂ @E-MoS₂ exhibited superior structural stability in both acidic and alkaline media, thereby enhancing the electrode's long-term catalytic activity and stability.

The superior catalytic activity and kinetics of MoO₂ @E-MoS₂ can be attributed to the synergistic advantage resulting from the preparation of 1 T/2 H mixed-phase MoS₂ with expanded layer spacing and the construction of heterogeneous structures. To confirm the superior catalytic performance of 1 T-MoS₂ over HER, we synthesized MoO₂ @E-MoS₂ with varying mass ratios of 2 H and 1 T phases through precise control of reaction temperatures at 170, 180, 190, and 220 °C (designated as MoO₂ @E-MoS₂-170, MoO₂ @E-MoS₂-180, MoO₂ @E-MoS₂-190, and MoO₂ @E-MoS₂-220). To determine the proportion of 1 T and 2 H MoS₂, we initially utilized S 2p spectra in XPS for peak splitting fitting. Subsequently, the areas under the peaks were employed to calculate their respective percentages (Fig. S22 and Table S2). As depicted in Fig. 5a, the MoO₂ @E-MoS₂-170, MoO₂ @E-MoS₂-180, MoO₂ @E-MoS₂-190, and MoO₂ @E-MoS₂-220 exhibited proportions of 1 T phase at 72.0%, 62.3%, 51.2%, and 0.0%, respectively. It is evident that the proportion of the 1 T-MoS₂ decreases with increasing temperature. At a temperature of 220 °C, the complete vulcanization of Mo–O bonds leads to all the MoS₂ in the sample becoming the more stable and thermodynamically favored hexagonal phase (2 H-MoS₂). In addition, the TG and DSC curves of MoO₂ @E-MoS₂-170, MoO₂ @E-MoS₂-190, and MoO₂ @E-MoS₂-220 were measured (Fig. S23). The calculation shows that the MoO₂ content in samples MoO₂ @E-MoS₂-170, MoO₂ @E-MoS₂-190, and MoO₂ @E-MoS₂-220 are 20.3 wt%, 8.9 wt%, and 3.7 wt%, respectively. In addition, the BET surface areas of MoO₂ @E-MoS₂-170, MoO₂ @E-MoS₂-180, MoO₂ @E-MoS₂-190, and MoO₂ @E-MoS₂-220 were measured. As shown in Fig. S24, the surface area of all four samples is approximately equal, ranging in size from 16.4 to 18.6 m² g⁻¹, suggesting that variations in vulcanisation temperature have negligible effects on the specific surface area. Even though the HER tests were conducted in 0.5 M H₂SO₄ and 1.0 M KOH (Fig. S25 and Fig. 5b), MoO₂ @E-MoS₂-180 still exhibits the lowest overpotential at any current density. Moreover, it can be observed that electrodes with higher content of 1 T phase demonstrate superior HER catalytic performance, except MoO₂ @E-MoS₂-170. Compared to MoO₂ @E-MoS₂-180, although the 1 T phase content in MoO₂ @E-MoS₂-170 is higher, the lower amount of generated MoS₂ at 170 °C during synthesis and poorer degree of crystallization result in unsatisfactory performance. In summary, the enhancement of 1 T phase content can significantly enhance the catalytic performance of the electrode. However, the properties of 1 T phase are not solely determined by its content but also influenced by other factors such as electrical conductivity, structural modification, and various other parameters.

3.3. DFT calculation

To illustrate the contribution of interlayer extended MoS₂ to the heightened activity of HER catalysts, we employed DFT calculations to determine the ΔE_{H20} , ΔG_H^* , and DOS of both pristine MoS₂ (0.62 nm) and E-MoS₂ electrodes (0.93 nm) with different layer spacing. Water

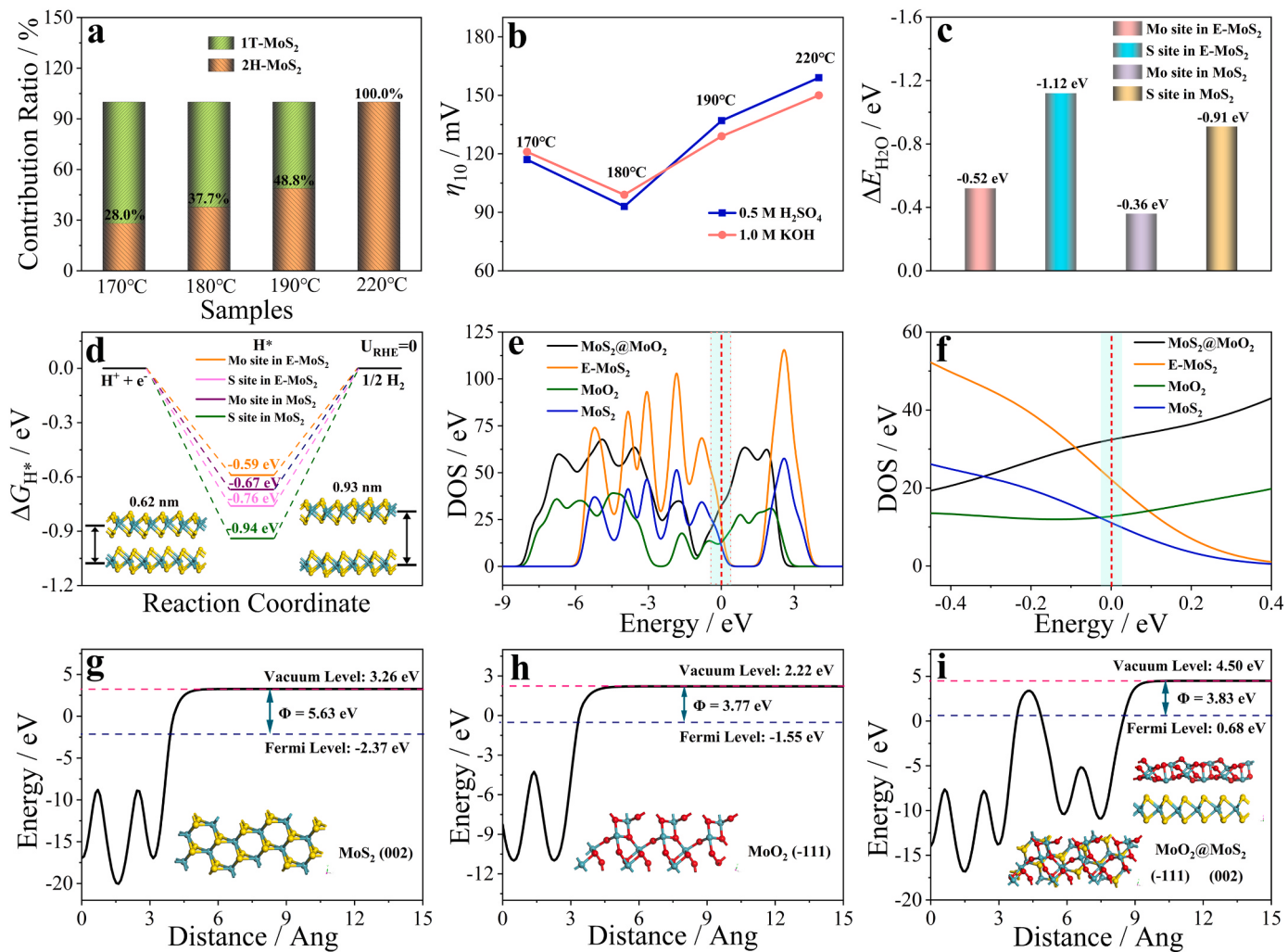


Fig. 5. a) Proportion of 1T-MoS₂ and 2H-MoS₂ content and b) η_{10} of MoO₂ @E-MoS₂-170, MoO₂ @E-MoS₂-180, MoO₂ @E-MoS₂-190, and MoO₂ @E-MoS₂-220. c) Adsorption energy of H₂O on the Mo or S site in MoS₂ and E-MoS₂. d) Structural model and calculated free energy diagrams of Mo or S site in MoS₂ and E-MoS₂. e,f) DOS of MoS₂, MoO₂, E-MoS₂, and MoO₂ @MoS₂. Work function of g) MoS₂, h) MoO₂, and i) MoO₂ @MoS₂.

molecules play a crucial role in the proton coupling/transfer kinetics during the HER process by acting as an effective proton donor on the electrocatalyst surface [36,37]. Therefore, we conducted further calculations to determine the $\Delta E_{\text{H}2\text{O}}$ of the Mo or S site in pristine MoS₂ and E-MoS₂. As depicted in Fig. 5c, Fig. S26, and Fig. S27, the $\Delta E_{\text{H}2\text{O}}$ values for the Mo and S sites in E-MoS₂ are -0.52 and -1.12 eV, respectively, which are more negative than those of the Mo and S sites in MoS₂ (-0.36 and -0.91 eV), indicating a higher propensity for H₂O adsorption on the interlayer-expanded structure. Interestingly, the S site is the primary adsorption site for H₂O, regardless of whether it is MoS₂ or E-MoS₂. Furthermore, DFT was utilized to further investigate the mechanisms that influence the expanded MoS₂ layer spacing and intrinsic electrocatalytic activity of hydrogen precipitation. The ΔG_{H}^* is a crucial parameter characterizing catalytic performance, and in the most ideal HER catalysts, ΔG_{H}^* approaches zero [38,39]. In comparison to the Mo site on MoS₂ (-0.76 eV) and S site on MoS₂ (-0.94 eV), as well as the Mo site in E-MoS₂ (-0.67 eV), Fig. 5d and Fig. S28 illustrate a ΔG_{H}^* value of -0.59 eV for the Mo site in E-MoS₂, indicating superior H^{*} adsorption/desorption capability for H₂ production. On one hand, E-MoS₂ exhibits a more optimized ΔG_{H}^* value than MoS₂ for both Mo and S sites, highlighting its superior HER activity after layer expansion. On the other hand, the optimized ΔG_{H}^* value of the Mo site in both MoS₂ and E-MoS₂ suggests that the catalytically active center of MoS₂ is located at its Mo site. Up to now, the DFT computational models of MoS₂ or E-MoS₂

indicate that the adsorption sites for water molecules and H are situated between the two layers of MoS₂. In order to assess the effect of different adsorption sites on the HER, we also conducted DFT calculations for the $\Delta E_{\text{H}2\text{O}}$ and ΔG_{H}^* associated with water molecules and H adsorbing onto the MoS₂ basal plane. As illustrated in Fig. S29, the S site in interlamination of E-MoS₂ exhibit a larger $\Delta E_{\text{H}2\text{O}}$ value of -1.12 eV than that of S site in MoS₂ basal plane (-1.04 eV), suggesting that S site in interlamination of E-MoS₂ are in favor of adsorbing water. Meanwhile, Mo site positioned at interlamination of E-MoS₂ exhibits a more optimized ΔG_{H}^* (-0.59 eV) compared to Mo site at the basal position (-0.66 eV), indicating that Mo sites in E-MoS₂ interlamination are more favorable for H adsorption and desorption (Fig. S30). In addition, the DOS for pristine MoS₂, and E-MoS₂ were calculated using DFT, as illustrated in Fig. 5e,f. Notably, E-MoS₂ exhibited a higher density of electronic states near the Fermi energy level, indicating that changes in electronic structure resulting from increased layer spacing can improve catalyst conductivity.

Strategies such as phase change engineering and modulation of layer spacing for MoS₂ have been demonstrated to enhance the HER catalytic activity of electrodes. Our next step is to investigate the impact of MoO₂ and MoS₂ heterojunctions (MoO₂ @MoS₂) on electrode catalytic performance. The work function (Φ) is a crucial parameter in the study of electron transfer between semiconductor heterostructures, and can be calculated as $\Phi = E_{\text{vac}} - E_f$, where E_{vac} represents vacuum energy and E_f

represents Fermi energy [40,41]. Therefore, to investigate electron transfer at the interface between MoS_2 and MoO_2 , we calculate the ϕ of MoS_2 , MoO_2 , and their heterostructure ($\text{MoO}_2 @\text{MoS}_2$) using this equation. As shown in Fig. 5g-i, the ϕ of MoS_2 (002), MoO_2 (-111), and $\text{MoO}_2 @\text{MoS}_2$ surfaces are measured to be 5.63, 3.77, and 3.83 eV, respectively. Upon formation of the $\text{MoO}_2 @\text{MoS}_2$ heterojunction, electrons will migrate from the MoO_2 surface to the MoS_2 surface until equilibrium is reached at a common Fermi energy level, and this electron transfer process is consistent with XPS results. To further investigate the charge transfer and separation patterns in the heterostructure, differential charge density analysis was conducted. The calculated differential charge density of the $\text{MoO}_2 @\text{MoS}_2$ heterojunction is presented in Fig. 6a. The cyan region denotes electron accumulation, while the pink region signifies electron depletion. This charge redistribution primarily occurs in proximity to the interface of MoS_2 and MoO_2 heterojunction, where electrons surrounding the Mo center in MoO_2 are transferred to S in neighboring MoS_2 . In addition, the DOS for monolayer MoS_2 , monolayer MoO_2 , and $\text{MoO}_2 @\text{MoS}_2$ were calculated using DFT, as illustrated in Fig. 5e,f. Notably, $\text{MoO}_2 @\text{MoS}_2$ exhibited a higher density of electronic states near the Fermi energy level, indicating faster electron transfer. The result suggests that heterostructure construction enhances the electrical conductivity of the material. In addition, in order to provide further evidence for the modulation of electronic structure, increasing the adsorption energy of water, and optimization of H^* adsorption/desorption performance through heterogeneous structure construction, we have conducted measurements on $\Delta E_{\text{H}_2\text{O}}$ and ΔG_{H}^* values at both Mo and S sites in monolayer MoS_2 , monolayer MoO_2 , and

$\text{MoO}_2 @\text{MoS}_2$. As shown in Fig. 6b, the $\Delta E_{\text{H}_2\text{O}}$ on the S site of MoS_2 in $\text{MoO}_2 @\text{MoS}_2$ (-1.32 eV) is comparatively lower than those of the Mo site in MoS_2 within $\text{MoO}_2 @\text{MoS}_2$ (-0.81 eV), Mo site of MoO_2 in $\text{MoO}_2 @\text{MoS}_2$ (-0.64 eV), Mo site of MoO_2 (-0.33 eV), Mo site of MoS_2 (-0.52 eV), and S site of MoS_2 (-1.05 eV). The aforementioned computed results not only demonstrate that the construction of heterogeneous structures can optimize water adsorption energy, which is conducive to enhancing HER catalytic activity, but also verify that the S site in the catalyst serves as the adsorption site for water. Moreover, Fig. S31 and Fig. S32 depicts the optimized cell model for each catalyst subsequent to hydrogen atom adsorption. The ΔG_{H}^* values of -0.94, -0.72, and -1.05 eV for the Mo site of MoO_2 , Mo site of MoS_2 , and S site of MoS_2 , respectively, suggest that the materials exhibit high adsorption strength and low desorption ability, which significantly impede the hydrogen production process (Fig. 6c). Additionally, the Mo site of MoS_2 in $\text{MoO}_2 @\text{MoS}_2$ (-0.22 eV) and the Mo site of MoO_2 in $\text{MoO}_2 @\text{MoS}_2$ (-0.53 eV) exhibit more optimized ΔG_{H}^* than the S site of MoS_2 in $\text{MoO}_2 @\text{MoS}_2$ (-0.81 eV), indicating that the catalytically active center of the $\text{MoO}_2 @\text{MoS}_2$ is located at the Mo site of MoS_2 (Fig. 6c). Notably, the Mo site of MoS_2 in $\text{MoO}_2 @\text{MoS}_2$ exhibits the smallest ΔG_{H}^* value (-0.22 eV) among all the Mo sites in both intrinsic state MoS_2 (0.72 eV) and MoO_2 (0.94 eV), once again demonstrating that the formation of a heterogeneous interface optimizes ΔG_{H}^* value of the electrode and thus enhances HER performance. In addition, we also conducted DFT calculations for the $\Delta E_{\text{H}_2\text{O}}$ and ΔG_{H}^* associated with water molecules and H adsorbing in interlamination and basal plane of $\text{MoO}_2 @\text{MoS}_2$. As illustrated in Fig. S33, the S site throughout MoO_2

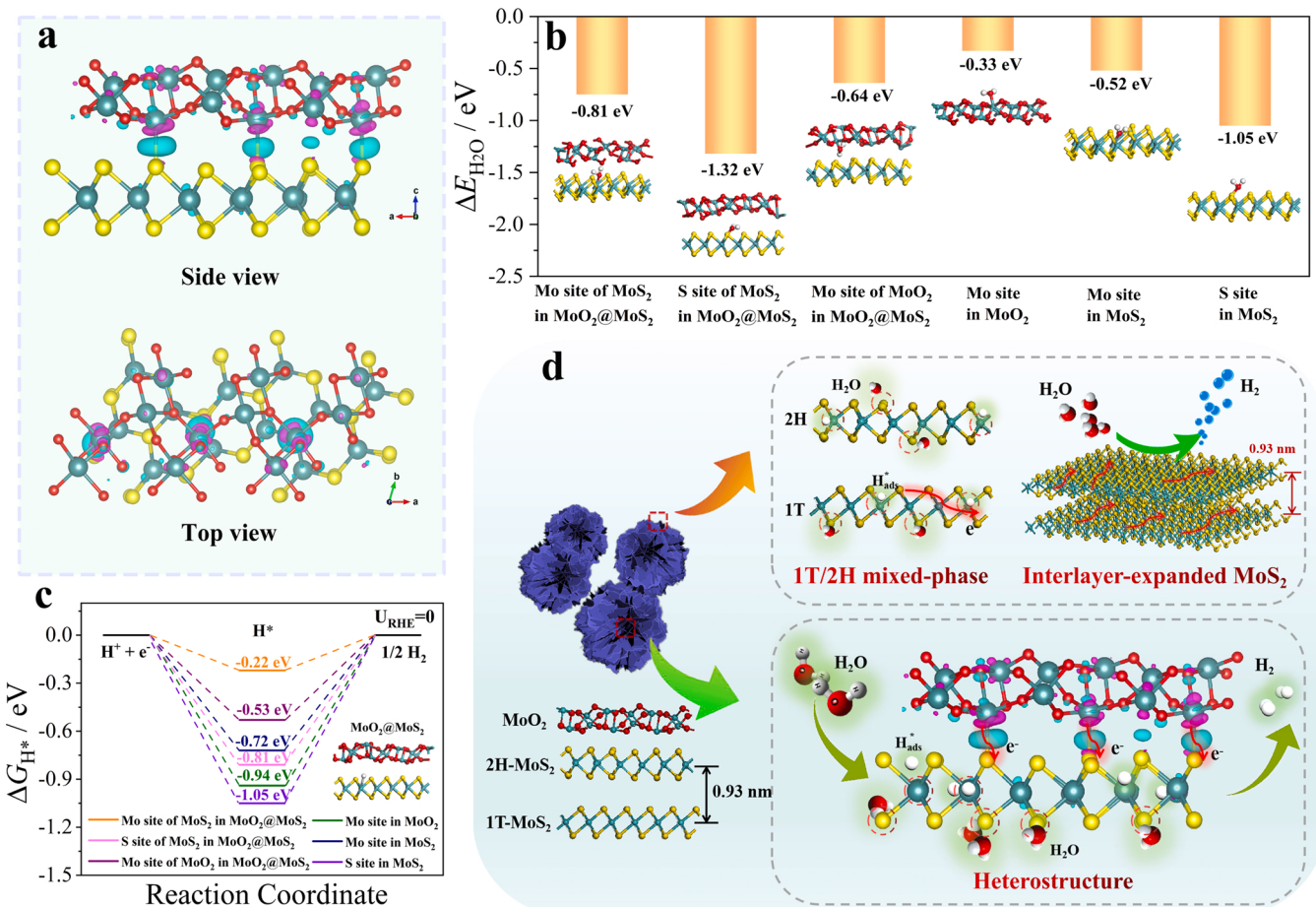


Fig. 6. a) Side view and top view of charge density difference in $\text{MoO}_2 @\text{MoS}_2$. Pink color represents charge depletion, while cyan color represents charge accumulation. b) Adsorption energy of H_2O and the corresponding DFT adsorption model of the Mo or S site in MoS_2 , MoO_2 , and $\text{MoO}_2 @\text{MoS}_2$. Oxygen is red, molybdenum is cyan, sulfur is yellow, and hydrogen is white, respectively. c) Calculated free energy diagrams of the Mo or S site in MoS_2 , MoO_2 , and $\text{MoO}_2 @\text{MoS}_2$ toward HER.

@MoS₂ exhibit significant $\Delta E_{\text{H}2\text{O}}$ values at both the interlamination (-1.32 eV) and basal plane (-1.38 eV), suggesting their favorable affinity for water adsorption. Moreover, for the basal plane of MoO₂@MoS₂ heterojunction, we also calculated the ΔG_{H}^* values of Mo site in MoO₂ and MoS₂. As shown in Fig. S34, Mo site of MoS₂ in MoO₂@MoS₂ interlamination has the smallest ΔG_{H}^* value of -0.22 eV than other materials, including Mo site of MoO₂ in MoO₂@MoS₂ interlamination (-0.53 eV), Mo site of MoS₂ in MoO₂@MoS₂ basal plane (-0.25 eV), and Mo site of MoO₂ in MoO₂@MoS₂ basal plane (-0.47 eV). This conclusion indicates that Mo site of MoS₂ in MoO₂@MoS₂ interlamination is more favorable for H adsorption and desorption. As a result, the above theoretical calculations indicate that the preparation of 1 T/2 H mixed-phase MoS₂ with expanded layer spacing and the construction of heterogeneous structures can modulate the electronic structure, improve the electrical conductivity, increase the $\Delta E_{\text{H}2\text{O}}$, and optimize the ΔG_{H}^* (Fig. 6d). Meanwhile, these results also confirm that water is adsorbed on the S site while H is adsorbed on the Mo site, which serves as the active center for facilitating rapid HER-catalyzed reaction (Fig. 6d).

4. Conclusion

In summary, we prepared interlayer expanded MoS₂ nanosheets with 1 T/2 H mixed-phase and constructed it with MoO₂ to form a heterostructure material through a solvothermal and thermal treatment approach. The presence of the 1 T phase and expanded layer structure of MoS₂ synergistically enhance electrode conductivity, increase active site exposure, promote H₂O adsorption, and optimize the ΔG_{H}^* . The constructed heterostructure can modulate the electronic structure of the catalyst, enhance electron transfer at the interface, optimize water adsorption energy, and reduce H* reaction energy barrier. DFT calculations reveal that the S site of MoS₂ in this catalyst exhibits a higher affinity towards H₂O adsorption, whereas the Mo site is more favorable for H* adsorption/desorption. As a result, it accelerates the thermodynamic and kinetic processes of catalytic reactions and enhances HER catalytic performance. The electrode's HER catalytic performance is enhanced, ultimately resulting in superior activity and stability of MoO₂@E-MoS₂. Specifically, MoO₂@E-MoS₂ demonstrates low overpotentials of 93 and 99 mV at a current density of 10 mA cm⁻², as well as exceptional long-term stabilities exceeding 70 and 130 h at current densities ranging from 10 to 30 mA cm⁻² in both acidic and alkaline media, respectively. Thus, our fundamental research with profoundly exploring the relationship between the structure and performance of MoS₂-based catalysts can provide theoretical guidance for the future design of high-performance HER electrocatalysts.

CRediT authorship contribution statement

Xianbo Yu conceived the project, designed the experiments, conducted the synthesis and characterizations, and tested the electrochemical performance. **Feng Yan, Xitian Zhang, and Yujin Chen** conceived and supervised the project. **Yang Zhao, Lili Wu, and Xinzhi Ma** wrote and edited the manuscript. **Bo Geng** conducted the theoretical calculations. All the authors discussed the results and commented on the manuscript.

Declaration of Competing Interest

We declare that we have no financial and personal relationships with other people or organizations that can inappropriately influence our work, there is no professional or other personal interest of any nature or kind in any product, service and/or company that could be construed as influencing the position presented in, or the review of, the manuscript entitled "A heterostructure of interlayer-expanded 1 T phase MoS₂ and spherical MoO₂ for efficient and stable hydrogen evolution".

Data availability

Data will be made available on request.

Acknowledgements

This work was supported by the Natural Science Foundation of Heilongjiang Province (No. LH2023B012 and LH2022B007), the National Natural Science Foundation of China (No. 22379034), and the Fundamental Research Funds for the Central Universities (No. 3072022QBZ2502 and 3072022TS2507).

Appendix A. Supporting information

Supplementary data associated with this article can be found in the online version at doi:10.1016/j.apcatb.2023.123534.

References

- [1] Y. Yang, P. Li, X. Zheng, W. Sun, S.X. Dou, T. Ma, H. Pan, Anion-exchange membrane water electrolyzers and fuel cells, Chem. Soc. Rev. 51 (2022) 9620, <https://doi.org/10.1039/d2cs00038e>.
- [2] A.H. Shah, Z. Zhang, Z. Huang, S. Wang, G. Zhong, C. Wan, A.N. Alexandrova, Y. Huang, X. Duan, The role of alkali metal cations and platinum-surface hydroxyl in the alkaline hydrogen evolution reaction, Nat. Catal. 5 (2022) 923–933, <https://doi.org/10.1038/s41929-022-00851-x>.
- [3] Q. Yang, H. Liu, P. Yuan, Y. Jia, L. Zhuang, H. Zhang, X. Yan, G. Liu, Y. Zhao, J. Liu, S. Wei, L. Song, Q. Wu, B. Ge, L. Zhang, K. Wang, X. Wang, C.-R. Chang, X. Yao, Single carbon vacancy traps atomic platinum for hydrogen evolution catalysis, J. Am. Chem. Soc. 144 (2022) 2171–2178, <https://doi.org/10.1021/jacs.1c10814>.
- [4] J. Ma, Z. Wang, B. Jiang, W. Wang, H. Wang, Directly imaging and regulating the nanoscale inhomogeneity of S-vacancies in molybdenum disulfide monolayer during electrocatalytic hydrogen evolution, Angew. Chem. Int. Ed. 62 (2023), e202305846, <https://doi.org/10.1002/anie.202305846>.
- [5] W. Han, J. Ning, Y. Long, J. Qiu, W. Jiang, Y. Wang, L.A. Shah, D. Yang, A. Dong, T. Li, Unlocking the ultrahigh-current-density hydrogen evolution on 2H-MoS₂ via simultaneous structural control across seven orders of magnitude, Adv. Energy Mater. 13 (2023), 2300145, <https://doi.org/10.1002/aenm.202300145>.
- [6] N. Solati, C. Karakaya, S. Kaya, Advancing the understanding of the structure-activity-durability relation of 2H-MoS₂ for the hydrogen evolution reaction, ACS Catal. 13 (2023) 342–354, <https://doi.org/10.1021/acscatal.2c03719>.
- [7] X. Guo, E. Song, W. Zhao, S. Xu, W. Zhao, Y. Lei, Y. Fang, J. Liu, F. Huang, Charge self-regulation in 1T'''-MoS₂ structure with rich S vacancies for enhanced hydrogen evolution activity, Nat. Commun. 13 (2022), 5954, <https://doi.org/10.1038/s41467-022-33636-8>.
- [8] Y. Chen, X. Wang, M. Lao, K. Rui, X. Zheng, H. Yu, J. Ma, S.X. Dou, W. Sun, Electrocatalytically inactive SnS₂ promotes water adsorption/dissociation on molybdenum dichalcogenides for accelerated alkaline hydrogen evolution, Nano Energy 64 (2019), 103918, <https://doi.org/10.1016/j.nanoen.2019.103918>.
- [9] Q. Wu, Y. Luo, R. Xie, H. Nong, Z. Cai, L. Tang, J. Tan, S. Feng, S. Zhao, Q. Yu, J. Lin, G. Chai, B. Liu, Space-confined one-step growth of 2D MoO₂/MoS₂ vertical heterostructures for superior hydrogen evolution in alkaline electrolytes, Small 18 (2022), 2201051, <https://doi.org/10.1002/smll.202201051>.
- [10] Y. Liu, Y. Chen, Y. Tian, T. Sakthivel, H. Liu, S. Guo, H. Zeng, Z. Dai, Synergizing hydrogen spillover and deprotonation by the internal polarization field in a MoS₂/NiPS₃ vertical heterostructure for boosted water electrolysis, Adv. Mater. 34 (2022), 2203615, <https://doi.org/10.1002/adma.202203615>.
- [11] Y. Chen, G. Meng, T. Yang, C. Chen, Z. Chang, F. Kong, H. Tian, X. Cui, X. Hou, J. Shi, Interfacial engineering of Co-doped 1T-MoS₂ coupled with V₂C MXene for efficient electrocatalytic hydrogen evolution, Chem. Eng. J. 450 (2022), 138157, <https://doi.org/10.1016/j.cej.2022.138157>.
- [12] Z. Xie, S. Yu, X. Ma, K. Li, L. Ding, W. Wang, D.A. Cullen, H.M. Meyer III, H. Yu, J. Tong, Z. Wu, F.-Y. Zhang, MoS₂ nanosheet integrated electrodes with engineered 1T–2H phases and defects for efficient hydrogen production in practical PEM electrolysis, Appl. Catal. B Environ. 313 (2022), 121458, <https://doi.org/10.1016/j.apcatb.2022.121458>.
- [13] K. Wang, K. Yu, S. Xu, S. Yuan, L. Xiang, B. Pang, J. Zheng, N. Li, Synergizing lattice strain and electron transfer in TMSs@1T-MoS₂ in-plane heterostructures for efficient hydrogen evolution reaction, Appl. Catal. B Environ. 328 (2023), 122445, <https://doi.org/10.1016/j.apcatb.2023.122445>.
- [14] Y. Zhang, T. Yang, J. Li, Q. Zhang, B. Li, M. Gao, Construction of Ru, O Co-doping MoS₂ for hydrogen evolution reaction electrocatalyst and surface-enhanced Raman scattering substrate: high-performance, recyclable, and durability improvement, Adv. Funct. Mater. 33 (2023), 2210939, <https://doi.org/10.1002/adfm.202210939>.
- [15] P. Zhang, H. Xiang, L. Tao, H. Dong, Y. Zhou, T.S. Hu, X. Chen, S. Liu, S. Wang, S. Garaj, Chemically activated MoS₂ for efficient hydrogen production, Nano Energy 57 (2019) 535–541, <https://doi.org/10.1016/j.nanoen.2018.12.045>.
- [16] L.A. Zavala, K. Kumar, V. Martin, F. Maillard, F. Maugé, X. Portier, L. Oliviero, L. Dubau, Direct evidence of the role of Co or Pt, Co single-atom promoters on the

- performance of MoS₂ nanoclusters for the hydrogen evolution reaction, *ACS Catal.* 13 (2023) 1221–1229, <https://doi.org/10.1021/acscatal.2c05432>.
- [17] X. Huang, M. Leng, W. Xiao, M. Li, J. Ding, T.L. Tan, W.S.V. Lee, J. Xue, Activating basal planes and S-terminated edges of MoS₂ toward more efficient hydrogen evolution, *Adv. Funct. Mater.* 27 (2017), 1604943, <https://doi.org/10.1002/adfm.201604943>.
- [18] C. Bie, B. Zhu, L. Wang, H. Yu, C. Jiang, T. Chen, J. Yu, A bifunctional CdS/MoO₂/MoS₂ catalyst enhances photocatalytic H₂ evolution and pyruvic acid synthesis, *Angew. Chem. Int. Ed.* 61 (2022), e202212045, <https://doi.org/10.1002/anie.202212045>.
- [19] M.-R. Gao, M.K.Y. Chan, Y. Sun, Edge-terminated molybdenum disulfide with a 9.4 Å interlayer spacing for electrochemical hydrogen production, *Nat. Commun.* 6 (2015), 7493, <https://doi.org/10.1038/ncomms8493>.
- [20] Y.-J. Tang, Y. Wang, X.-L. Wang, S.-L. Li, W. Huang, L.-Z. Dong, C.-H. Liu, Y.-F. Li, Y.-Q. Lan, Molybdenum disulfide/nitrogen-doped reduced graphene oxide nanocomposite with enlarged interlayer spacing for electrocatalytic hydrogen evolution, *Adv. Energy Mater.* 6 (2016), 1600116, <https://doi.org/10.1002/aenm.201600116>.
- [21] X. Yu, F. Yan, B. Geng, X. Bai, C. Zhao, M. Wang, Y. Zhao, G. Zhao, X. Zhang, Role of introduced Se element and induced anion vacancies in Mo(SSe)₂- \sqrt{G} van der Waals heterostructure for enhanced hydrogen evolution reaction, *J. Colloid Interf. Sci.* 633 (2023) 155–165, <https://doi.org/10.1016/j.jcis.2022.11.080>.
- [22] L. Diao, B. Zhang, Q. Sun, N. Wang, N. Zhao, C. Shi, E. Liu, C. He, An in-plane Co₉S₈@MoS₂ heterostructure for the hydrogen evolution reaction in alkaline media, *Nanoscale* 11 (2019) 21479–21486, <https://doi.org/10.1039/c9nr06609h>.
- [23] H.D. Mai, S. Jeong, G.-N. Bae, N.M. Tran, J.-S. Youn, C.-M. Park, K.-J. Jeon, Pd sulfidation-induced 1T-phase tuning in monolayer MoS₂ for hydrogen evolution reaction, *Adv. Energy Mater.* 13 (2023), 2300183, <https://doi.org/10.1002/aenm.202300183>.
- [24] H. Zhang, H. Xu, L. Wang, C. Ouyang, H. Liang, S. Zhong, A metal-organic frameworks derived 1T-MoS₂ with expanded layer spacing for enhanced electrocatalytic hydrogen evolution, *Small* 19 (2023), 2205736, <https://doi.org/10.1002/smll.202205736>.
- [25] X. Li, S. Han, Z. Qiao, X. Zeng, D. Cao, J. Chen, Ru monolayer island doped MoS₂ catalysts for efficient hydrogen evolution reaction, *Chem. Eng. J.* 453 (2023), 139803, <https://doi.org/10.1016/j.cej.2022.139803>.
- [26] Z. Liu, L. Zhao, Y. Liu, Z. Gao, S. Yuan, X. Li, N. Li, S. Miao, Vertical nanosheet array of 1T phase MoS₂ for efficient and stable hydrogen evolution, *Appl. Catal. B Environ.* 246 (2019) 296–302, <https://doi.org/10.1016/j.apcatb.2019.01.062>.
- [27] Z. Lei, J. Zhan, L. Tang, Y. Zhang, Y. Wang, Recent development of metallic (1T) phase of molybdenum disulfide for energy conversion and storage, *Adv. Energy Mater.* 8 (2018), 1703482, <https://doi.org/10.1002/aenm.201703482>.
- [28] B. Chen, D. Chao, E. Liu, M. Jaroniec, N. Zhao, S.-Z. Qiao, Transition metal dichalcogenides for alkali metal ion batteries: engineering strategies at the atomic level, *Energy Environ. Sci.* 13 (2020) 1096–1131, <https://doi.org/10.1039/c9ee03549d>.
- [29] S. Gong, G. Zhao, P. Lyu, K. Sun, Insights into the intrinsic capacity of interlayer expanded MoS₂ as a Li-ion insertion host, *J. Mater. Chem. A* 7 (2019) 1187–1195, <https://doi.org/10.1039/c8ta08120d>.
- [30] X. Yu, G. Zhao, H. Huang, C. Liu, P. Lyu, N. Zhang, Interlayer-expanded MoS₂ nanoflowers anchored on the graphene: a high-performance Li⁺/Mg²⁺ co-intercalation cathode material, *Chem. Eng. J.* 428 (2022), 131214, <https://doi.org/10.1016/j.cej.2021.131214>.
- [31] S. Gong, G. Zhao, P. Lyu, K. Sun, A pseudolayered MoS₂ as Li-ion insertion host with enhanced rate capability and durability, *Small* 14 (2018), 1803344, <https://doi.org/10.1002/smll.201803344>.
- [32] C. Yu, Y. Shi, F. Yan, Y. Zhao, C. Zhu, X. Zhang, X. Zhang, Y. Chen, Three-dimensional FeP nanotube arrays fabricated through electrostatic-repulsion-limited-nucleation strategy for high-efficiency hydrogen evolution, *Chem. Eng. J.* 423 (2021), 130240, <https://doi.org/10.1016/j.cej.2021.130240>.
- [33] E. Hu, Y. Yao, Y.I. Chen, Y. Cui, Z. Wang, G. Qian, Boosting hydrogen generation by anodic oxidation of iodide over Ni-Co(OH)₂ nanosheet arrays, *Nanoscale Adv.* 3 (2021) 604–610, <https://doi.org/10.1039/d0na00847h>.
- [34] X. Yu, G. Zhao, S. Gong, C. Liu, C. Wu, P. Lyu, G. Maurin, N. Zhang, Design of MoS₂/graphene van der Waals heterostructure as highly efficient and stable electrocatalyst for hydrogen evolution in acidic and alkaline media, *ACS Appl. Mater. Interfaces* 12 (2020) 24777–24785, <https://doi.org/10.1021/acsmami.0c04838>.
- [35] B. Geng, F. Yan, X. Zhang, Y. He, C. Zhu, S.-L. Chou, X. Zhang, Y. Chen, Conductive CuCo-based bimetal organic framework for efficient hydrogen evolution, *Adv. Mater.* 33 (2021), 2106781, <https://doi.org/10.1002/adma.202106781>.
- [36] Y. Luo, Z. Zhang, F. Yang, J. Li, Z. Liu, W. Ren, S. Zhang, B. Liu, Stabilized hydroxide-mediated nickel-based electrocatalysts for high-current-density hydrogen evolution in alkaline media, *Energy Environ. Sci.* 14 (2021) 4610–4619, <https://doi.org/10.1039/dlee01487k>.
- [37] Z. Chen, Y. Xu, D. Ding, G. Song, X. Gan, H. Li, W. Wei, J. Chen, Z. Li, Z. Gong, X. Dong, C. Zhu, N. Yang, J. Ma, R. Gao, D. Luo, S. Cong, L. Wang, Z. Zhao, Y. Cui, Thermal migration towards constructing W-W dual-sites for boosted alkaline hydrogen evolution reaction, *Nat. Commun.* 13 (2022), 763, <https://doi.org/10.1038/s41467-022-28413-6>.
- [38] L. Li, P. Wang, Q. Shao, X. Huang, Metallic nanostructures with low dimensionality for electrochemical water splitting, *Chem. Soc. Rev.* 49 (2020) 3072–3106, <https://doi.org/10.1039/d0cs00013b>.
- [39] Y.-N. Zhou, F.-L. Wang, J. Nan, B. Dong, H.-Y. Zhao, F.-G. Wang, N. Yu, R.-N. Luan, D.-P. Liu, Y.-M. Chai, High-density ultrafine RuP₂ with strong catalyst-support interaction driven by dual-ligand and tungsten-oxygen sites for hydrogen evolution at 1 A cm⁻², *Appl. Catal. B Environ.* 304 (2022), 120917, <https://doi.org/10.1016/j.apcatb.2021.120917>.
- [40] H. Huang, G. Zhao, X. Sun, X. Yu, C. Liu, X. Shen, M. Wang, P. Lyu, N. Zhang, Built-in electric field enhanced ionic transport kinetics in the T-Nb₂O₅@MoO₂ heterostructure, *J. Mater. Chem. A* 9 (2021) 22854–22860, <https://doi.org/10.1039/dita06599h>.
- [41] D. Chen, R. Lu, R. Yu, Y. Dai, H. Zhao, D. Wu, P. Wang, J. Zhu, Z. Pu, L. Chen, J. Yu, S. Mu, Work-function-induced interfacial built-in electric fields in Os-OsSe₂ heterostructures for active acidic and alkaline hydrogen evolution, *Angew. Chem. Int. Ed.* 61 (2022), e202208642, <https://doi.org/10.1002/ange.202208642>.